Journal of Materials Chemistry A

Reversible Oxygen Intercalation in Hexagonal $Y_{0.7}Tb_{0.3}MnO_{3+\delta}$: Toward Oxygen Production by Temperature-Swing Absorption in Air

Journal:	*Journal of Materials Chemistry A*
Manuscript ID	TA-ART-09-2018-009235.R2
Article Type:	Paper
Date Submitted by the Author:	12-Dec-2018
Complete List of Authors:	Klimkowicz, Alicja; Shibaura Institute of Technology - Toyosu Campus, SIT Research Laboratories Cichy, Kacper; Akademia Gorniczo-Hutnicza imienia Stanislawa Staszica w Krakowie Chmaissem, Omar; Northern Illinois University, Department of Physics Dabrowski, Bogdan; Northern Illinois University, Department of Physics Poudel, Bisham ; Northern Illinois University, Department of Physics Świerczek, Konrad; AGH University of Science and Technology, Faculty of Energy and Fuels, Department of Hydrogen Energy; AGH University of Science and Technology, AGH Centre of Energy Taddei, Keith; Oak Ridge National Laboratory, Neutron Scattering Division Takasaki, Akito; Shibaura Institute of Technology - Toyosu Campus, Department of Engineering Science and Mechanics

Reversible Oxygen Intercalation in Hexagonal $Y_{0.7}Tb_{0.3}MnO_{3+\delta}$: Toward Oxygen Production by Temperature-Swing Absorption in Air

Alicja Klimkowicz[1,#], Kacper Cichy[2], Omar Chmaissem[3], Bogdan Dabrowski[3,$], Bisham Poudel[3], Konrad Świerczek[2,4], Keith M. Taddei[5], Akito Takasaki[6]

[1]Shibaura Institute of Technology, SIT Research Laboratories,

3-7-5 Toyosu, Koto-ku, 135-8548 Tokyo, Japan

[2]AGH University of Science and Technology, Faculty of Energy and Fuels, Department of Hydrogen Energy, al. A. Mickiewicza 30, 30-059 Krakow, Poland

[3]Northern Illinois University, Department of Physics, DeKalb, IL 60115, USA

[4]AGH Centre of Energy, AGH University of Science and Technology, ul. Czarnowiejska 36, 30-054 Krakow, Poland

[5]Neutron Scattering Division, Oak Ridge National Laboratory, Oak Ridge, TN 37831, USA

[6]Shibaura Institute of Technology, Department of Engineering Science and Mechanics,

3-7-5 Toyosu, Koto-ku, 135-8548 Tokyo, Japan

[#]alicja@shibaura-it.ac.jp

[$]dabrowski@anl.gov

KEYWORDS Oxygen storage; Temperature-swing process; Hexagonal $RMnO_{3+\delta}$ oxides; X-ray diffraction; Neutron diffraction; Thermogravimetic Analysis

ABSTRACT: Oxygen storage capacity, structure and thermodynamic stability were studied for hexagonal $Y_{0.7}Tb_{0.3}MnO_{3+\delta}$ in oxygen and air to assess its applicability for oxygen separation from air by temperature-swing adsorption process. We show that large amounts of oxygen excess can be reversibly incorporated into and extracted from small particle-size samples of $Y_{0.7}Tb_{0.3}MnO_{3+\delta}$

prepared by sol-gel synthesis for fixed oxygen partial pressures. The hyperstoichiometric material, with $\delta \geq 0.45$ prepared in oxygen or high-pressure oxygen atmospheres, assumes a new hexagonal structure with interstitial oxygen defects near the nominally five coordinated Mn site as determined by neutron diffraction and supplemented with scanning and transmission electron microscopy. Thermogravimetric measurements demonstrate reversible intercalation of oxygen in pure O_2 atmosphere around 300 °C, but more importantly, also in air over a remarkably narrow temperature range of ~20 °C, albeit producing smaller oxygen amounts $\delta \leq 0.25$. Comparison of samples' properties obtained by the sol-gel and solid-state synthesis methods confirms enhanced oxygen storage capacity and oxygen exchange kinetics for the small particle-size samples which exhibit larger specific surface area. Sequential temperature-swing absorption and the long-term annealing experiments demonstrate the high practical potential of $Y_{0.7}Tb_{0.3}MnO_3$ compounds for the industrial production of oxygen enriched gases by utilization of waste heat at 250 - 350 °C.

1. Introduction

Society demand for pure or highly enriched oxygen gas is constantly increasing. This trend is expected to continue as oxygen's applications in a wide range of industrial and medical uses continues to grow. Most of such oxygen used is obtained by cryogenic distillation from air. This process is fairly expensive due to the high upfront capital costs required by the complex facilities and large energy consumption needed for gas liquefaction [1]. Moreover, the ever-growing restrictions and regulations related to environmental concerns and energy efficiency motivate the development of novel, low-cost technologies for oxygen production. Other more efficient but not widely used production methods include pressure-swing adsorption techniques and gas separation by polymeric and, more recently, by ceramic membranes [2, 3]. A new promising alternative to the cryogenic oxygen production technology is air separation by temperature-swing adsorption (TSA) [4]. In TSA materials possessing the ability to selectively adsorb atmospheric oxygen are harnessed to produce

usable high purity oxygen. This method is particularly interesting due to its simplicity and functionality at slightly elevated temperature ranges which allows the recovery and effective use of heat usually wasted by various industrial processes.

With their ability to reversibly incorporate/release oxygen into/from their structure, oxygen storage materials (OSM) can be regarded among the best possible candidates for application using TSA methods. It should be underlined that the oxygen incorporation/release process in OSMs is a bulk property instead of being merely a surface effect; therefore, the effective oxygen extraction process is due to absorption rather than adsorption.

Since the 1980s, ceria stabilized zirconia (CeO_2-ZrO_2) [5] has become widely used in three-way catalysts designed for gasoline-fueled vehicles. Albeit attractive, the oxygen storage capacity (OSC) of stabilized zirconia registered during pressure swings rarely exceeded 0.5 mmol-O_2/g [6, 7], which is a relatively low value. Since 2010 there has been significant interest in the introduction of transition metal oxides for such applications. For example, double perovskite $BaYMn_2O_{5+\delta}$ is a candidate OSM material, which, due to layered arrangement of the Ba and Y cations in the *A*-sublattice, allows for a fast lattice oxygen exchange [8]. Oxygen incorporation/reduction processes for this compound occur fast and reversibly at a temperature of approximately 500 °C with a change in the oxygen partial pressure ranging between air and 5 vol.% H_2 in Ar ($pO_2 \leq 10^{-16}$ atm). Practical OSC values reach 1 mmol-O_2/g (> 3.5 wt.%), which corresponds to changes of the oxygen stoichiometry (δ) of up to 1 mole of oxygen (O) per mole of compound [9, 10]. However, such materials are not well-suited for oxygen production because the reductive step involves hydrogen and produces water instead of oxygen. However, materials working in Pressure-Swing Adsorption (PSA) mode can be suitable as sorbents as it was shown for $SrCo_xFe_{1-x}O_{3-\delta}$ [11].

Recent research [12-22] has shown that it is possible to develop efficient OSMs for oxygen separation using TSA methods at fixed oxygen pressure. For example, $Ca_2Al_{1-x}Ga_xMnO_{5+\delta}$ brownmillerite shows a high oxygen storage capacity of ~3.0 wt % in oxygen. Unfortunately, the operation

temperature of this material is above 550 °C making it difficult to use for practical applications [21]. In the related perovskite (Ba,Sr)$Co_{0.8}Fe_{0.2}O_{3-\delta}$, substitution of cobalt and iron on the B-site, translates into a lower temperature of absorption, however this only reduces the operation temperature to 500 °C [18]. The complex cobalt oxide $YBaCo_4O_{7+\delta}$ was shown to operate at lower temperatures (below 400 °C) however, the temperature difference ΔT between reduction and oxidation temperatures is quite large ~ 150-350 °C, which could hinder practical application [16, 17]. Excitingly, the recently proposed, $R$$MnO_{3+\delta}$ (with R = rare earth) hexagonal materials can work in oxygen at a range of temperatures on the order of 200-350°C suggesting their possible use as potential TSA materials. These rare earth manganites have similar OSC to the fast ion exchange material $BaYMn_2O_{5+\delta}$. As summarized by Parkkima's doctoral dissertation [1], development of these hexagonal manganites for low temperature oxygen extraction in air creates possibilities for their use in other diverse technological applications [23] such as the three-way-catalysts with improved efficiency of operation [24], thermochemical dissociation of water [25] or decomposition of nitrogen oxides [26]. Modern energy-generating technologies such as chemical looping combustion [27], fuel cell technology [28], and production of syngas and hydrogen through partial oxidation of natural gas [29-31] can also benefit from the application of effective OSMs. The main challenges that remain for OSM to become fully operational are to improve: the OSC in air, the kinetics of the oxygen intake/release process in the proper temperature range, and the long-term reversibility of the method.

Depending on the size of the R^{3+} cation and the oxygen partial pressure during synthesis, rare earth $R$$MnO_{3+\delta}$ manganites usually crystallize in either a perovskite structure for the larger lanthanides, (La-Dy) or a hexagonal structure for the smaller lanthanides (Ho-Lu, Y and Sc) [11, 12]. Oxygen stoichiometric phases (δ = 0), denoted as Hex0, crystallize in the hexagonal $P6_3cm$ symmetry which can be described as a layered structure in which layers of R^{3+} cations in eight-fold coordination are separated by layers of corner-sharing trigonal $Mn^{3+}O_5$ bipyramids. Such a coordination for the $3d^4$ Mn orbitals causes splitting of electronic orbitals into three sets: a' (d_{z2}), e' (d_{x2-y2}, d_{xy}), and e'' (d_{xz},

d_{yz}) with high-spin states of e'^2 and e'^2. Shortening of the Mn-O apical bond lengths occurs in the trigonal bipyramids as a consequence of electronic band filling with four electrons and results in a number of interesting physicochemical properties. A very important property, from the viewpoint of TSA, is the possibility of the introduction of a significant amount of interstitial oxygen into the structure near the Mn site, which increases the Mn valence to above 3+. This process leads to creation of a unique, maximally eightfold coordination of the manganese cations and changes the symmetry of the primitive cell. Introduction of interstitial oxygen into the structure results in the formation of oxygen-loaded phases having different symmetries: *R*3*c* ($\delta \approx 0.28$, Hex1) and *Pca*2$_1$ ($\delta \approx 0.41$, Hex2), as described in previous reports [12, 14].

The temperature range of oxygen exchange and the OSC properties can be effectively tuned for the RMnO$_{3+\delta}$ oxides by partial substitution of large rare earth metals in the *R*-sublattice [14, 15, 32]. As another approach to improving the OSC, previous work demonstrated that significant enhancements of oxygen kinetics and practical OSC can be achieved in materials with sub-micrometric size of particles as in YMnO$_{3+\delta}$, for example [33]. We have recently shown that materials prepared by the sol-gel (SG) technique exhibit significantly smaller particle size than that obtained using routine high temperature solid-state reaction synthesis methods (SS). This should lead to improved kinetic properties during operation in oxygen atmosphere [33, 34].

In this work, we use thermogravimetric and diffraction measurements to report the superior oxygen extraction and storage properties of a novel family of terbium substituted YMnO$_{3+\delta}$ materials, $Y_{1-x}Tb_xMnO_{3+\delta}$, obtained using the sol-gel and solid-state synthesis methods. The highly oxygenated $Y_{0.7}Tb_{0.3}MnO_{3.45}$ exhibits a new hexagonal structure (Hex3 - space group *P*6$_3$*mc*), which we describe in this paper based on neutron diffraction and electron microscopy data.

2. Experimental details

2.1. Materials Preparation

Hexagonal $Y_{0.7}Tb_{0.3}MnO_{3+\delta}$ materials were synthesized using two different methods: the typical, high-temperature solid state method (sample denoted as YTMO SS) and the sol-gel method (sample denoted as YTMO SG). For the solid-state method, a 4 gram stoichiometric mixture of MnO_2, Tb_2O_3 and Y_2O_3 was mechanically milled in ethanol for 12 h in a zirconia container. The resulting homogenous slush was left to dry on a hot plate for 2 days. The dried powder was then ground and annealed in air at 1000 °C for 12 hours, ground again, pressed into two 2 g pellets and annealed in Ar at 1350 °C for 12 hours. One pellet was used for initial annealing experiments in air, oxygen, Ar and high oxygen pressure, and subsequently studied by X-ray powder diffraction, electron microscopy and thermogravimetric measurements. These experiments showed reversible oxygen content changes and structural transformations between Hex0, Hex1, and a newly observed phase defined here as Hex3. The Hex2 phase was not observed during these annealing. The second pellet was prepared for neutron powder diffraction experiments. It was annealed in high oxygen pressure at 245 atm. at 400 °C and then slow cooled to room temperature at 0.1 °C min^{-1}. The final oxygen content was determined to be $\delta \approx 3.47$ from the mass change.

The soft chemistry SG method was used in order to obtain materials with smaller grain size. Cation stoichiometric $Y(NO_3)_3 \cdot 6H_2O$, $Tb(NO_3)_3 \cdot 6H_2O$ and $Mn(NO_3)_2 \cdot 4H_2O$ were dissolved in a small amount of deionized water and combined with a premixed complexing agent solution of ethylenediaminetetraacetic acid dissolved in ammonia. The mixture was poured into a quartz evaporator and heated in atmospheric air, up to about 400 °C to evaporate water, enable sol-gel transition for the decomposition of ammonium nitrate as well as the oxidation of residual carbon. The as-prepared precursor was ground and pressed into pellets with a thickness of about 1 mm and a diameter of about 10 mm. Final synthesis of the materials was performed in a tube furnace at 1050 °C, for 8 h in an atmosphere of 5N Ar, with a gas flow of about 50 cm^3 min^{-1}.

2.2. Materials Characterization

Initial structural studies of the synthesized oxides conducted at room temperature were carried out using a Panalytical Empyrean X-ray diffractometer in a 10-110 deg. range (2θ) with CuK_α radiation ($K\alpha_1$ = 1.54056 Å and $K\alpha_2$ = 1.54439 Å). High-temperature measurements were performed using Anton Paar HTK 1200N oven-chamber. Temperature dependent measurements in air were conducted with a speed of 50 min per scan and a 5 °C min^{-1} heating rate between the measurements.

Neutron powder diffraction experiments were performed on the high-resolution time-of-flight diffractometer POWGEN at the Spallation Neutron Source and at the constant wavelength diffractometer HB-2A at the High Flux Isotope Reactor of Oak Ridge National Laboratory [35]. The GSAS/EXPGUI software suite was used for Rietveld analysis of the X-ray and neutron data [36, 37]. In the final refinement cycles, all variables were allowed to refine including lattice parameters, scale factor, background, profile parameters and the atomic parameters listed in Table 1. VESTA software was used for preparation of the crystal structure illustrations [38].

Powder morphology and chemical composition evaluations with element-specific mapping were conducted using a JEOL / JSM-7610F scanning electron microscope equipped with energy dispersive X-ray spectroscopy. High resolution transmission electron microscopy (TEM) imaging was conducted using JEOL / JEM-2100 equipped with wolfram emitter, at an accelerating voltage of 200 kV.

Thermogravimetric analysis (TG) was performed to determine the oxygen production properties of our materials such as oxygen storage capacity and oxygen intake and release kinetics. Experiments were performed using TA Q5000 IR apparatus. All the measurements were conducted on powdered 20 mg samples evenly distributed on a shallow platinum pan with a direct flow of 100 cm^3 min^{-1} gas on the sample. Measurements of the oxygen content dependence on temperature were performed with heating and cooling rates of 0.1-5 °C min^{-1}. Before each measurement, the investigated samples were

heated to 500 °C then cooled to room temperature with a heating rate of 5 °C min^{-1} in flowing air to remove moisture. This process produces slightly oxidized starting samples for some of the TG measurements. The material's performance was evaluated in several 30 min. time segments of alternating reduction and oxidation processes during temperature swings between 300 °C and 350 °C in O_2. Temperature changes were induced with heating and cooling rates of 100 °C min^{-1}. Performance in air was evaluated during 300 min. isothermal oxidation at various temperatures between 230-310 °C followed by 30 min. reduction at 330 °C. The following notation is used for denoting oxygen stoichiometry: if the absolute value of the oxygen content in the respective materials is known, it is given (e.g. 3 in the stoichiometric $Y_{0.7}Tb_{0.3}MnO_3$); for multiphase hexagonal materials or if the data concern dynamical process with changing oxygen content, $Y_{0.7}Tb_{0.3}MnO_{3+\delta}$ notation is used.

3. Results and Discussion

3.1 Samples Characterization and Structural Studies

X-ray diffraction patterns of the as-synthesized $Y_{0.7}Tb_{0.3}MnO_3$ SS and SG samples are shown in Figure 1 together with Rietveld refinement best-fits. Select structural parameters are presented in Table S1. The oxygen stoichiometry of the as-synthesized materials is close to $\delta = 0$ which suggests the Hex0 phase which crystallizes in the $P6_3cm$ space group [14]. This structure was used in the refinement and shows excellent agreement with the observed diffraction patterns of the single-phase samples. As can be seen from SEM micrographs in Figure 2a-d, both the SS-YTMO and SG-YTMO powders show irregular shapes of primary and secondary particles, and as expected, the SS synthesis method yields larger primary particles of ~10 μm size. The SG synthesis method gives much smaller primary particles of ~1 μm, which are connected and forming porous agglomerates of less than 20 μm in size. Similar influence of the preparation method on morphology was shown previously for

$YMnO_{3+\delta}$ [33]. Moreover, both powders show a homogeneous distribution of the constituent elements (Figures S1 and S2).

Investigation of the thermal expansion behavior of the as-prepared $Y_{0.7}Tb_{0.3}MnO_3$ (Hex0, $P6_3cm$) sample in air revealed the same tendency of the unit cell parameters as observed in the unsubstituted Ho- and Y-containing materials where c and a decrease and increase respectively with increasing temperature. [33, 34]. Linear thermal expansion coefficients (TEC) were evaluated from unit cell volume changes: $TEC_{25\text{-}500°C} = 11.7(2) \cdot 10^{-6}\ K^{-1}$ and $TEC_{500\text{-}800°C} = 12.3(1) \cdot 10^{-6}\ K^{-1}$ (Figure 3), and are slightly different than the TEC of the Ho- and Y-containing materials which are $TEC^{YMnO3+\delta}{}_{25\text{-}500°C} = 10.7(2) \cdot 10^{-6}\ K^{-1}$ and $TEC^{YMnO3+\delta}{}_{500\text{-}800°C} = 12.8(1) \cdot 10^{-6}\ K^{-1}$ [33]. At 900 °C, the $P6_3cm$ structure appears to undergo a structural phase transition to higher symmetry. As seen in the insert of Figure 3, diffraction peaks at 22.5 deg, 35.75 deg and 36.75 deg disappear above 900 C. Good refinement of this structure was obtained using the aristotype $P6_3/mmc$ space group symmetry (a = 3.6210(1), c = 11.3482(2), Rw_p = 3.8%) reported for the $YMnO_3$ material [33]. The room temperature $P6_3cm$ symmetry of the oxygen stoichiometric $Y_{0.7}Tb_{0.3}MnO_3$ phase (Hex0) can be described as due to cooperative displacive distortions that lower the $P6_3/mmc$ symmetry of the ordered higher temperature parent phase [39-41].

3.2. Structural Properties of New $Y_{0.7}Tb_{0.3}MnO_{3.45}$ Hex3 Phase.

After annealing at 400 C in a high oxygen pressure of 245 atm., the the Hex0 phase underwent major changes. Considering the persistence of the Hex0 phase's main Bragg reflections in the Hex3 diffraction patterns in addition to the appearance of new Hex3 peaks, it is reasonable to assume that the two structures are symmetry related. Therefore, we used ISODISTORT [42] to perform initial symmetry-mode irreducible representation analyses using $P6_3/mmc$ as our starting parent symmetry from which structural distortions due to oxygen occupancy, atomic displacements and strains were

allowed. As the new reflections in the Hex3 phase where commensurate with a doubling of the Hex0 phase's a and b lattice parameters, we restricted our search to space groups with unit cells doubled along the *a*- and *b*- directions. No restrictions were made regarding the possible symmetry of the daughter structure. With these conditions, our search produced a handful of possible space group candidates that all, except one ($P6_3mc$), failed to produce decent fits to the data. The $P6_3mc$ model discussed below, which served well as a starting point, produced an excellent fit to the neutron diffraction data (see Figure 4) and reasonable bond-lengths and polyhedral coordination. Moreover, it allowed for stable and physically meaningful refinement of atomic parameters for most of the atoms, especially oxygen, which were found to move significantly away from their originally generated positions.

Coherent neutron scattering lengths for Y and Tb are 7.75 and 7.38 fm, respectively and so provide very little contrast for neutron diffraction. Therefore, refinement of the relative site occupancies, with or without constraints, was not possible using our neutron diffraction data. Refinement of the Y site occupancy gave the same fractional value of 0.93(2) for both the independent Y1 and Y2 sites which is consistent, within less than three standard deviations, with the expected average scattering length of a site occupied by $Y_{0.7}Tb_{0.3}$. Refinement of the oxygen site occupancies resulted in sites being completely full except for the equatorial in-plane atoms O1 and O2. These two mobile atoms had to shift the most with site occupancies reduced to about 90 and 92%, respectively. While the O1 and O2 sites are nearly full giving rise to the structure shown in Figure 5 (d-f). vacancies must exist as determined in our refinements to accommodate the interstitial oxygen atoms O5 which we identify in this study. Fully occupied sites would otherwise produce unreasonable in-plane O-O distances. For simplicity and clarity, the partially occupied O5 (0 0 z; z~0.29) site (~35%) shown as red and white circles in Figures. 5 (d and e) was not used in the construction of the Mn and (Y/Tb) polyhedra. It is interesting to notice the remarkable agreement between the refined total oxygen content $O_{3.45}$ and that observed with mass changes and thermogravimetric analysis. It is also worth mentioning that an

alternative site suitable for oxygen interstitials at the center of the upright equilateral triangles forming between the octahedral Mn at (1/3 2/3 z with z~0.29) is completely empty, thus, emphasizing the site-selective oxygen insertion and the associated structural ordering. Structural data and select bond-lengths are listed in Table 1 and Table 2, respectively. The larger than usual anisotropic thermal factors for Mn2 and O5 are in agreement with structures that contain similar partially occupied interstitial sites as in the cuprate superconductors and other oxides [43-46], for example. Although unphysical, we note that the small refined negative U_{33} component of the Mn thermal factor is within less than two standard deviations which makes it essentially zero. No changes to the structure were detected when setting this term to some arbitrarily small positive value or zero. Comparison with the stoichiometric Hex0 phase demonstrates that that the high levels of oxygen nonstoichiometry at low temperatures is due to presence of small size Mn cation with mixed oxidation state susceptible to variable coordination which allows oxygen anion accommodation in its neighborhood.

The structure of the Hex0 oxygen stoichiometric parent phase consists of alternating layers of corner-sharing MnO_5 bipyramids and edge-sharing YO_7 polyhedra as shown in Figure 5 a). The Mn layer offers wide channels suitable for easy diffusion of oxygen into the structure. Excess oxygen O5 goes into the Mn layer at a reasonable distance from both the Mn and (Y/Tb) ions, Figure 5 (d and e). The presence of O5 in this layer forces O1 and O2 to move significantly away from their original positions to convert three out of four Mn bipyramids into corner-shared octahedra as shown in Figure 5 e). Comparing Figures 5 b) and e), one can easily observe the formation of an ordered pattern created by hexagonal rings of six Mn octahedra surrounding the unconverted Mn bipyramids. Likewise, only one out of four yttrium polyhedra converts to an YO_9 polyhedron surrounded by six unconverted YO_7 polyhedra in a similarly ordered fashion. As such, the structure of the new oxygen loaded $Y_{0.7}Tb_{0.3}MnO_{3.45}$ material consists of alternating Y and Mn layers that contain two independent Y or Mn sites, respectively. The highly-oxidized Hex3 phase was also detected in $Y_{0.7}Tb_{0.3}MnO_{3.45}$ SG sample after thermogravimetric measurement in oxygen pressure of 1 atm. The

XRD data together with refined structural parameter can be found in Figure S3 and Table S2. A TEM image of the new structure, viewing along the (200) plane is presented in Figure S4.

3.3. Improved OSC in Hexagonal Manganites by Introduction of Terbium.

As shown in our previous publications [12, 14, 15, 33, 34], the temperature of oxygen intake correlates with the size of the rare earth element in the *A*-sublattice. With an increase of the average ionic size the stability of excess oxygen in hexagonal manganites rises to higher temperatures, which increases kinetics of intake and release of oxygen. More importantly the OSC increases significantly in the vicinity of a structural stability boundary between the hexagonal and perovskite phases. We found that in terbium substituted hexagonal $YMnO_3$ materials, this separation boundary is achieved with the composition $Y_{0.5}Tb_{0.5}MnO_3$. Unfortunately, achieving the single-phase material required several prolonged firings in high purity Ar. In this paper, we have chosen thus to focus on studying the OSC properties of $Y_{0.7}Tb_{0.3}MnO_3$ composition due to practical reasons of easier synthesis.

Thermogravimetric measurements in oxygen (Figure 6a and b) are conducted as described in our previous work [33, 34] and with the initial annealing experiments described earlier. Maximum oxygen (O) intakes of 0.37 mole and 0.45 mole were observed for the $Y_{0.7}Tb_{0.3}MnO_3$ SS and $Y_{0.7}Tb_{0.3}MnO_3$ SG, respectively, with heating/cooling rate of 0.1 °C min^{-1}. The oxygen intake/release is smaller for faster heating/cooling rates however, as previously observed, the smaller particle size of YTMO SG allows more oxygen absorption and larger intake values even when faster heating/cooling rates are applied [33, 34]. To the best of our knowledge, the oxygen storage capacity, presented in Table 3, of Tb substituted samples is the highest among all the rare-earth substituted $Y_{1-x}R_xMnO_{3+\delta}$ materials reported to date. More importantly, the significant OSC enhancement in our materials correlates well with the appearance of the oxygen-loaded Hex3 phase. Consistent with the average ionic size increase, the 30% substitution of the larger terbium cations on the smaller yttrium increases the

temperature corresponding to maximum oxygen content on heating from 225 °C for $YMnO_{3+\delta}$ to 286 °C (see Table 3) as well as the temperatures of incorporation and release of oxygen. Further, the temperature difference between oxidation and reduction processes showed a record low ΔT value ~20 °C, which is very promising for potential TSA applications.

To evaluate the potential applicability of our materials for TSA processes, thermogravimetric tests of reversible oxidation/reduction were performed. A fully oxidized $Y_{0.7}Tb_{0.3}MnO_{3.45}$ SG sample was rapidly (100 °C min^{-1}) heated in pure O_2 to 350 °C. At this temperature, the material started to release the stored oxygen. After 30 min. at 350 °C, the sample was cooled to 300 °C and kept in such conditions for another 30 min. which caused its partial re-oxidation in agreement with Figure 6b. Figure 7 shows ten consecutive cycles of oxygen intake and release by the material at 300 °C and 350 °C, respectively. The oxygen absorption and desorption curves for every cycle are compared separately in Figures. S5a and b, respectively. The TG curves are almost straight lines over the entire 30 min oxidation time which indicates that this time interval was not sufficient to utilize the full capacity of the material. Additional *in situ* XRD and TG experiments show that achieving equilibrium oxygen excess content of δ = 0.45 would require longer annealing for several hours. The oxygen desorption curves show faster kinetics as expected when taking into account the higher temperature used for oxygen reduction. Equilibrium excess oxygen contents of δ = 0.02 were achieved at 350 °C after 10-15 min.

The oxygen content change during heating and cooling stabilized only after the first 2 cycles due to the high initial oxygen content of δ = 0.45, which would require annealing longer than 30 min. to achieve the equilibrium oxygen content at 350 °C of δ = 0.02. The subsequent oxygen content changes were completely reproducible in the range of 0.155-0.165 during heating and cooling as it is shown in Table S3. By assuming δ changes of 0.16 during the full 45 min. cycle (30 min. for oxidation and 15 min. reduction) 1 mole of material could deliver 0.08 mole of O_2; therefore, 1 tonne of $Y_{0.7}Tb_{0.3}MnO_3$ (4,7 kmole) in analogous conditions should be able to deliver about 375 moles of O_2

(or 8.4 m^3/cycle) which is equal to a daily (32 cycles/day) production of around 270 m^3. It should be noted that these oxygen production amounts could be further enhanced by optimizing the temperatures and times of the oxygen intake and release.

Considering their proven potential for TSA oxygen production applications, the effective operation of hexagonal $Y_{1-x}R_xMnO_{3+\delta}$ in air is desired. TG curves shown on Figures. 8a and b, recorded during the slowest heating/cooling runs in air demonstrate an oxygen intake δ of 0.142 (1.06 wt.%) and 0.246 (1.81 wt.%) for the YTMO SS and the YTMO SG samples, respectively, once again proving the advantages of the smaller particle size achieved with SG synthesis. As shown in Table 4, this result is very promising as to date, because the best air performance data published in the literature showed $\delta = 0.08$ (i.e. OSC = 0.50 wt.%) for small grain $HoMnO_{3+\delta}$ SS achieved after 15 min. of ball milling, while pure $YMnO_3$ did not show any excess oxygen during annealing in air [33, 34]. Similar to the TG results in oxygen, Figure 8a and b demonstrate that YTMO SG has a narrower working oxidation/reduction temperature range as well as faster kinetics than its YTMO SS counterpart.

In an attempt to find the best temperature conditions for oxygen production in air, preliminary isothermal measurements of the kinetics of the oxygen intake and release for the $Y_{0.7}Tb_{0.3}MnO_{3+\delta}$ SG sample were performed at temperatures between 230 – 310 °C and at 330 °C, as shown in Figures 9a and b. The fastest rate of oxidation in air was found at ~270 °C, which was the same temperature as found by the maximum of the derivative of the TG cooling oxygen content curve at cooling rate of 0.1 °C min^{-1} (Figure 8b). The kinetics of the oxygen intake in air are noticeably slower than those in oxygen (see Figure 7 and Figure 6b) as the temperature of oxidation in air (~270 °C) is significantly lower than in oxygen (~325 °C, as estimated by the maximum of the derivative of the TG cooling oxygen content curve at cooling at a rate of 0.1 °C min^{-1} shown in Figure 6b vs temperature). Comparison of the fast oxidation whilst achieving equilibrium oxygen content at 310 °C in ~ 30 min. (Figure 9a) with the fast reduction whilst achieving equilibrium oxygen content at 330 °C in ~ 10

min. (Figure 9b) demonstrate the remarkably narrow temperature range of ~ 20 °C for oxidation/reduction process.

The times of oxygen reduction at 330 °C, which depend on the initial oxygen content, are not much different than in oxygen and could be further shortened at higher temperatures. The slower oxygen intake kinetics and the similar reduction kinetics in air and oxygen, are expected because of the lower oxygen partial pressure of air. Clearly, while times of the oxygen reduction can be shortened and the equilibrium content lowered by increasing temperature above 330 °C, the oxidation step in air is limiting fast production of oxygen and further studies should focus on improvement of the oxidation process. Nevertheless, analogous to the performance evaluations in oxygen, using 1 ton of $Y_{0.7}Tb_{0.3}MnO_3$ SG and assuming single working cycle of 315 min in air (300 min for oxidation and 15 min for reduction) leads to the production of almost 25 m^3 of pure O_2 per day. These oxygen production amounts could be further improved by shortening working cycle with a better choice of the oxidation/reduction temperatures and the use of smaller substitution amounts of a heavy Tb in $YMnO_3$.

Finally, we investigated the OSC and long-term stability of our materials by keeping the YTMO SG sample at 265 °C for 45 hours in flowing air followed by an isothermal reduction test at 330 °C as shown in Figure S6. The oxygen content increased to $\delta = 0.38$, and during 30 min. reduction process the sample released ~0.18 mole of oxygen (O) consistent with reduction dependent on the initial oxygen content shown on Figure 9b, thus demonstrating the long-term stability and reproducibility of oxygen exchange in air.

4. Conclusions

We have shown that partial substitution of Y by Tb in hexagonal $Y_{0.7}Tb_{0.3}MnO_{3+\delta}$ allows for the formation of a new highly oxygen-loaded Hex3 phase when the materials is annealed both in a pure

oxygen environment ($\delta = 0.45$), and in air ($\delta = 0.25$). Oxygen loading occurs at temperatures suitable for swing processes using waste heat around 300°C. Thermogravimetric measurements confirmed the reversible intercalation of oxygen, high OSC and fast kinetics of the oxidation and reduction processes in air in comparison with $Y_{1-x}Dy_xMnO_{3+\delta}$ and $HoMnO_{3+\delta}$ [15, 33, 34]. Thus, these materials exhibit a strong potential for production of oxygen enriched gases by utilization of waste heat generated at industrial facilities such as coal and natural gas burning power plants and steel mills. For example, the onsite use of OSM to enrich an oxygen nitrogen gas blend from 20% O_2/N_2 to 30% O_2/N_2 would offer significant efficiency improvements by reducing the amount of heated gases used in the process, as well as by decreasing CO_2 emission. Further optimization of the hexagonal manganates' OSC could be pursued by substituting smaller amounts of larger size rare earth elements in $YMnO_3$ at the perovskite/hexagonal phase separation boundary. Such substitutions are reasonably expected to increase the oxygenation/reduction operating temperatures and, thus, to speed up the kinetics of oxygen exchange which result in shorter oxygenation/reduction working cycles.

The discovered Hex3 phase shows significant concentration of the interstitial oxygen defects at the equatorial sites near the Mn sites. Oxygen hopping between interstitial sites is known to be activated at lower temperatures than hopping between the oxygen vacancy sites, as seen for example in perovskites, because of a smaller hopping energy barrier. However, because interstitial oxygen defects are localized near the Mn sites in hexagonal manganites, which indicates strong bonding, the hopping energy barrier is apparently not that much different than in oxygen deficient perovskites, as indicated by the similar temperatures of oxygen exchanges. The remarkable advantage of hexagonal manganites relies on very large oxygen content changes that can be achieved over small intervals of operating temperatures.

ACKNOWLEDGEMENTS

Part of this work was supported by JSPS KAKENHI Grant Number JP18K13997. A portion of this research performed at ORNL's High Flux Isotope Reactor and the Spallation Neutron Source was sponsored by the Scientific User Facilities Division, Office of Basic Energy Sciences, US Department of Energy. Part of this project was funded by the National Science Centre, Poland, on the basis of the decision number UMO-2015/19/B/ST8/00871.

REFERENCES

1. Parkkima, O.; $YBaCo_4O_{7+\delta}$ and $YMnO_{3+\delta}$ Based Oxygen-Storage Materials. *Doctoral dissertation, Aalto University,* 2014.

2. Bhide, B. D.; Stern, A. A new evaluation of membrane processes for the oxygen-enrichment of air. II. Effects of economic parameters and membrane properties. *J. Membrane Sci.* 1991, *62*, 37-58.

3. Da Costa, J.; Smart, S.; Motuzas, J.; Liu, S.; Zhang, D. State of Art (SOTA) Report on Dense Ceramic Membranes for Oxygen Separation from Air. 2013, 1-18.

4. Abughayada, C.; Air Separation and Oxygen Storage Properties of Hexagonal Rare-Earth Manganites, *Doctoral dissertation, Northern Illinois University*, 2015.

5. Kašpar, J.; Fornasiero, P.; Graziani, M. Use of CeO_2-based oxides in the three-way catalysis. *Catalysis Today* 1999, *50*, 285-298.

6. Raju, V.; Jaenicke, S.; Chuah, G. -K. Effect of hydrothermal treatment and silica on thermal stability and oxygen storage capacity of ceria–zirconia. *Applied Catalysis B: Environmental* 2009, *91*, 92-100.

7. He, H.; Dai, H. X.; Au, C. T. Defective structure, oxygen mobility, oxygen storage capacity, and redox properties of RE-based (RE = Ce, Pr) solid solutions. *Catalysis Today* 2004, *90*, 245-254.

8. Motohashi, T.; Ueda, T.; Masubuchi, Y.; Takiguchi, M.; Setoyama, T.; Oshima, K.; Kikkawa, S. Remarkable Oxygen Intake/Release Capability of $BaYMn_2O_{5+\delta}$: Applications to Oxygen Storage Technologies. *Chem. Mater.* 2010, *22*, 3192-3196.

9. Klimkowicz, A.; Świerczek, K.; Takasaki, A.; Molenda, J.; Dabrowski, B. Crystal structure and oxygen storage properties of $BaLnMn_2O_{5+\delta}$ (Ln: Pr, Nd, Sm, Gd, Dy, Er and Y) oxides *Mater. Res. Bull.* 2015, *65*, 116-122.

10. Klimkowicz, A.; Świerczek, K.; Yamazaki, T.; Takasaki, A. Enhancement of the oxygen storage properties of $BaPrMn_2O_{5+\delta}$ and $BaSmMn_2O_{5+\delta}$ oxides by a high-energy milling. *Solid State Ionics* 2016, *298*, 66-72.

11. Ikeda, H.; Tsuchida, A.; Morita, J.; Miura, N. $SrCo_xFe_{1-x}O_{3-\delta}$ Oxygen Sorbent Usable for High-Temperature Pressure-Swing Adsorption Process Operating at Approximately 300 °C. *Ind. Eng. Chem. Res.* 2016, *55*, 6501- 6505.

12. Abughayada, C.; Dabrowski, B.; Remsen, S.; Kolesnik, S.; Chmaissem, O. Structural, magnetic, and oxygen storage properties of hexagonal $Dy_{1-x}Y_xMnO_{3-\delta}$. *J. Solid State Chem.* 2014, *217*, 127-135.

13. Parkkima, O.; Malo, S.; Hervieu, M.;. Rautama, E. –L.; Karppinen, M. New $RMnO_{3+\delta}$ (R = Y, Ho; $\delta \approx 0.35$) phases with modulated structure. *J. Solid State Chem.* 2015, *221* 109-115.

14. Abughayada, C.; Dabrowski, B.; Kolesnik, S.; Brown, D. E.; Chmaissem, O. Characterization of Oxygen Storage and Structural Properties of Oxygen-Loaded Hexagonal $RMnO_{3+\delta}$ (R = Ho, Er, and Y). *Chem. Mater.* 2015, *27(18)*, 6259-6267.

15. Remsen, S.; Dabrowski, B. Synthesis and Oxygen Storage Capacities of Hexagonal $Dy_{1-x}Y_xMnO_{3-\delta}$. *Chem. Mater.* 2011, *23*, 3818-3827.

16. Karppinen, M.; Yamauchi, H.; Otani, S.; Fujita, T.; Motohashi, T.; Huang, Y.-H.; Valkeapää, M.; Fjellvåg, H. Oxygen Nonstoichiometry in $YBaCo_4O_{7+\delta}$: Large Low-Temperature Oxygen Absorption/Desorption Capability. *Chem. Mater.* 2006, *18*, 490-494.

17. Parkkima, O.; Karppinen, M. The $YBaCo_4O_{7+\delta}$-Based Functional Oxide Material Family: A Review. *Eur. J. Inorg. Chem*. 2014, *15*, 4056-4067.

18. Yufeng He, Y.; Zhu, X.; Li, Q.; Yang, W. Perovskite Oxide Absorbents for Oxygen Separation. *AIChE Journal*, 2009, *55*, 3125-3133.

19. Vieten, J.; Bulfin, B.; Call, F.; Lange, M.; Schmucker, M.; Francke, A.; Roeb, M.; Sattlera, C. Perovskite oxides for application in thermochemical air separation and oxygen storage. *J. Mater. Chem. A*, 2016, *4*, 13652-13659.

20. Bulfin, B.; Vieten, J.; Starr, D. E.; Azarpira, A.; Zachaus, C.; Havecker, M. Skorupska, K.; Schmucker, M.; Roeb, M.; Sattler, C. Redox chemistry of $CaMnO_3$ and $Ca_{0.8}Sr_{0.2}MnO_3$ oxygen storage perovskites. *J. Mater. Chem. A*, 2017, *5*, 7912-7919.

21. Motohashi, T.; Hirano, Y.; Masubuchi, Y.; Oshima, K.; Setoyama, T.; Kikkawa S.; Oxygen Storage Capability of Brownmillerite-type $Ca_2AlMnO_{5+\delta}$ and Its Application to Oxygen Enrichment. *Chem. Mater.* 2013, *25*, 372-377.

22. Motohashi, T.; Kimura, M.; Inayoshi, T.; Ueda, T.; Masubuchi, Y.; Kikkawa S. Redox characteristics variations in the cation-ordered perovskite oxides $BaLnMn_2O_{5+\delta}$ (Ln = Y, Gd, Nd, and La) and $Ca_2Al_{1-x}Ga_xMnO_{5+\delta}$ ($0 \leq x \leq 1$) *Dalton Trans.* 2015, *33*, 10746-10752.

23. Shelley, S. Oxygen and Nitrogen: Onward and Upward. *Chem. Eng. Prog.* 2009, *105*, 6-18.

24. Guilhaume, N.; Primet, M. Three-Way Catalytic Activity and Oxygen Storage Capacity of Perovskite $LaMn_{0.976}Rh_{0.024}O_{3+\delta}$. *J. Catal.* 1997, *165*, 197-204.

25. Kodama, T.; Gogon, N. Thermochemical Cycles for High-Temperature Solar Hydrogen Production. *Chem. Rev.* 2007, *107*, 4048-4077.

26. Jiang, H.; Wang, H.; Liang, F.; Werth, S.; Schiestel, T.; Caro, J. Direct Decomposition of Nitrous Oxide to Nitrogen by In Situ Oxygen Removal with a Perovskite Membrane. *Angew. Chem. Int.* 2009, *48*, 2983-2986.

27. Rydén, M.; Lyngfelt, A.; Mattisson, T.; Chen, D.; Holmen, A.; Bjorgum, E. Novel oxygen-carrier materials for chemical-looping combustion and chemical-looping reforming; $La_xSr_{1-x}Fe_yCo_{1-y}O_{3-\delta}$ perovskites and mixed-metal oxides of NiO, Fe_2O_3 and Mn_3O_4. *Int. J. Greenhouse Gas Control* 2008, *2*, 21-36.

28. Xu, Z.; Qi, Z.; Kaufman, A. Effect of oxygen storage materials on the performance of proton-exchange membrane fuel cells. *J. Power Sources* 2003, *115*, 40-43.

29. Li, K.; Wang, H.; Wei, Y.; Yan, D. Partial oxidation of methane to syngas with air by lattice oxygen transfer over ZrO_2-modified Ce–Fe mixed oxides. *Chem. Eng. J.* 2011, *173*, 574-582.

30. Kado, S.; Imagawa, K. -I.; Kiryu, A.; Yagi, F.; Minami, T.; Kawai, H.; Kawazuishi, K.-I.; Tomishige, K.; Nakamura, A.; Suehiro, Y. Syngas production from natural gas via catalytic partial oxidation using ceramic monolith catalyst at short contact time and elevated pressure. *Catal. Today* 2011, *171*, 97-103.

31. Dai, X. P.; Wu, Q.; Li, R. J.; Yu, C. C.; Hao, Z. P. Hydrogen Production from a Combination of the Water-Gas Shift and Redox Cycle Process of Methane Partial Oxidation via Lattice Oxygen over LaFeO3 Perovskite Catalyst. *J. Phys. Chem.* 2006, *110*, 25856-25862.

32. Dabrowski, B.; Remsen, S.; Mais, J.; Kolesnik, S. Synthesis and Characterization of Non-Stoichiometric Hexagonal $Dy_{1-x}Y_xMnO_{3-\delta}$. *Funct. Mater. Lett.* 2011, *4(2)*, 147-150.

33. Klimkowicz, A.; Świerczek, K.; Kobayashi, S.; Takasaki, A.; Allahyani, W.; Dabrowski, B. Improvement of oxygen storage properties of hexagonal $YMnO_{3+\delta}$ by microstructural modifications. *J. State Chem.* 2018, *258*, 471-476.

34. Świerczek, K.; Klimkowicz, A.; Nishihara, K.; Kobayashi, S.; Takasaki, A.; Alanizy, M.; Kolesnik, S.; Dabrowski, B.; Seonge, S.; Kange, J. Oxygen storage properties of hexagonal $HoMnO_{3+\delta}$. *Phys. Chem. Chem. Phys.* 2017, *19*, 19243-19251.

35. Calder, S.; An, K.; Boehler, R.; Dela Cruz, C. R.; Frontzek, M. D.; Guthrie, M.; Haberl, B.; Huq, A.; Kimber, S. A. J.; Liu, J.; Molaison, J. J.; Neuefeind, J.; Page, K.; dos Santos, A. M.; Taddei, K. M.; Tulk, C.; Tucker M. G. A suite-level review of the neutron powder diffraction instruments at Oak Ridge National Laboratory. *Rev. Sci. Instrum.* 2018, *89*, 092701 1-16

36. Larson, A.C.; von Dreele, R.B. GSAS General Structure Analysis System. Los Alamos Natl. Lab. Rep. – LAUR 2004, 86-748.

37. Toby, H.B. EXPGUI, a graphical user interface for GSAS. *J. Appl. Cryst.* 2001, 210-213.

38. Momma, K.; Izumi, F. VESTA 3 for three-dimensional visualization of crystal, volumetric and morphology data. *J. Appl. Crystallogr*. 2011, *44*, 1272-1276.

39. Gibbs, A. S.; Knight, K. S.; Lightfoot, P. High-temperature phase transitions of hexagonal YMnO3. *Phys. Rev. B* 2011, *83*, 094111-1-9.

40. Jeong, I. -K.; Hurb, N. Proffen, Th. High-temperature structural evolution of hexagonal multiferroic $YMnO_3$ and $YbMnO_3$. *J. Appl. Cryst.* 2007, *40*, 730-734.

41. Łukaszewicz, K.; Karut-Kalicińska, J. X-Ray investigations of the crystal structure and phase transitions of $YMnO_3$. *Ferroelectrics* 1974, *7*, 81-82.

42. Campbell, B. J.; Stokes, H. T.; Tanner, D. E.; Hatch, D. M. ISODISPLACE: a web-based tool for exploring structural distortions. *J. Appl. Cryst.* 2006, *39*, 607-614.

43. Jorgensen, J. D.; Dabrowski, B.; Shiyou Pei, Hinks, D. G.; Soderholm, L.; Morosin, B.; Schiber, J. E.; Venturini E. L.; Ginley, D. S. Superconducting phase of $La_2CuO_{4+\delta}$: A superconducting composition resulting from phase separation. *Phys. Rev. B*, **1988**, *38*, 11337-11345.

44. Sharma, R.; Ganguly, Y. R.; Rajagopal, H.; Sequeira, A.; Yakhimi, J. V.; Dasannnacharya, B. A. Neutron Structural Investigations of $Y_{1-x}Ca_xBa_2Cu_{3-y}Co_yO_{7\pm\delta}$. *J. Supercond.* 1995, *8*, 271-277.

45. Galati, R.; Hughes, R. W.; Knee, C. S.; Henry, P. F.; Weller, M. T. The structure of superconducting $RbOs_2O_6$ between 2 K and 300 K. *J. Mater. Chem.* 2007, *17*,160-163.

46. De la Calle, C. Alonso, J. A. Aguadero, A. Fernández-Díaz, M. T. Phase transformations in $Sr_{0.8}Ba_{0.2}CoO_{2.5}$ brownmillerite: correlationbetween structure and transport properties. *Dalton T.* 2009, *21*, 4104-4114.

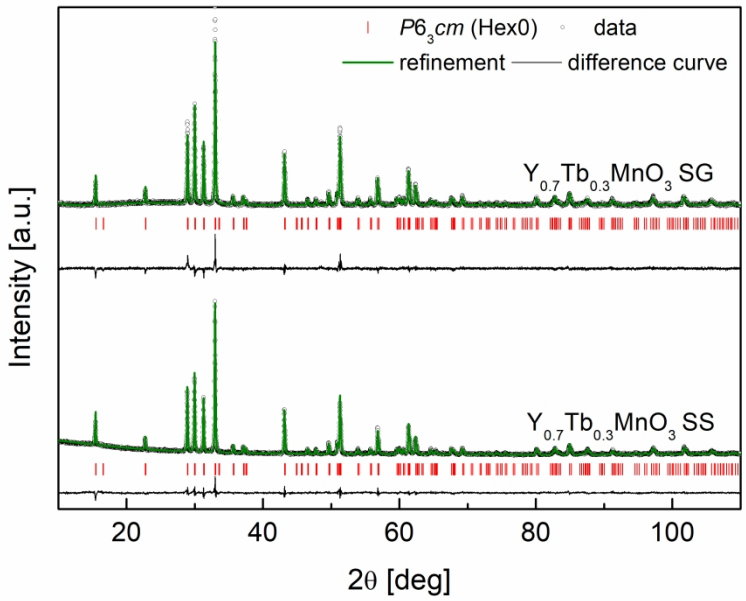

Figure 1. Room temperature XRD data for the as-synthesized $Y_{0.7}Tb_{0.3}MnO_3$ SS and SG samples together with best-fit Rietveld refinements.

288x201mm (300 x 300 DPI)

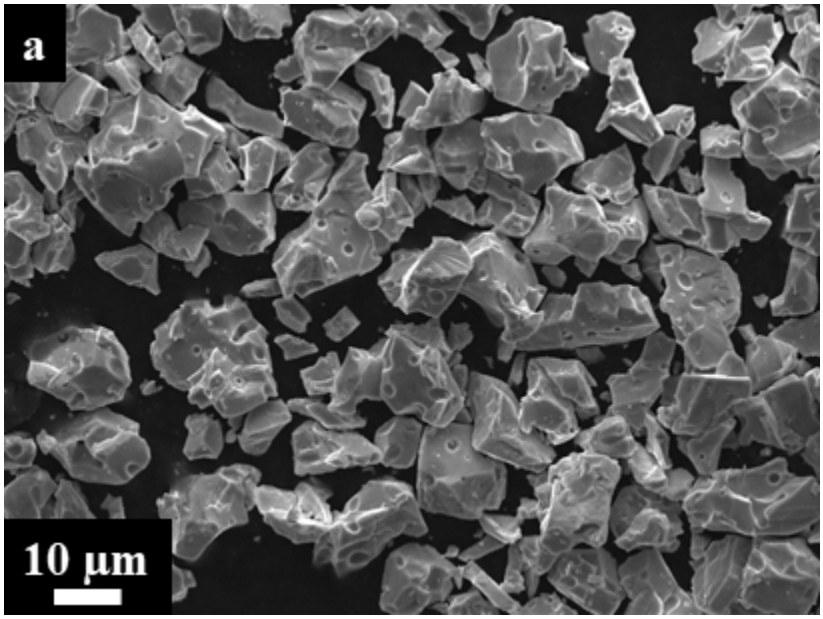

Figure 2. SEM micrographs for $Y_{0.7}Tb_{0.3}MnO_3$ powders: YTMO SS magnification a) 1000, b) 10000 and YTMO SG magnification c) 1000, d) 10000.

107x80mm (96 x 96 DPI)

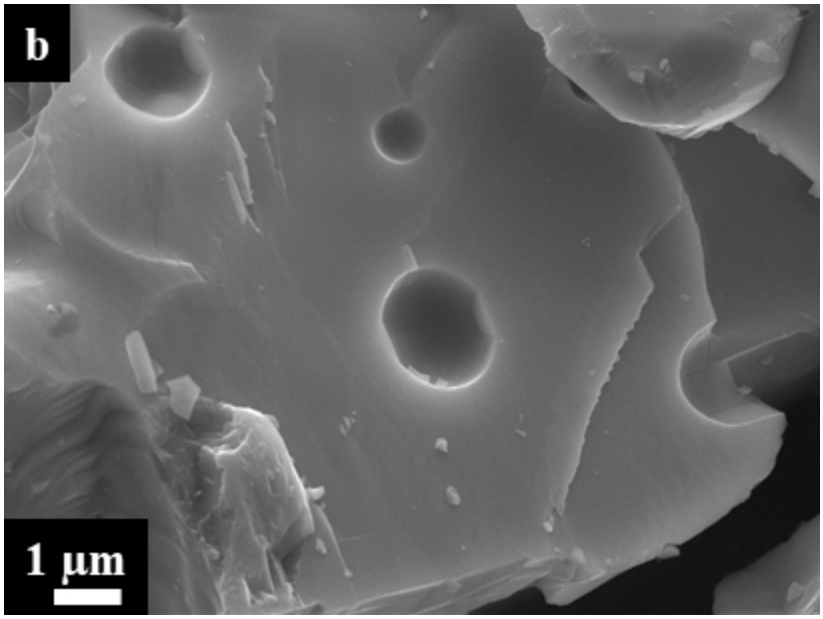

Figure 2. SEM micrographs for $Y_{0.7}Tb_{0.3}MnO_3$ powders: YTMO SS magnification a) 1000, b) 10000 and YTMO SG magnification c) 1000, d) 10000.

107x80mm (96 x 96 DPI)

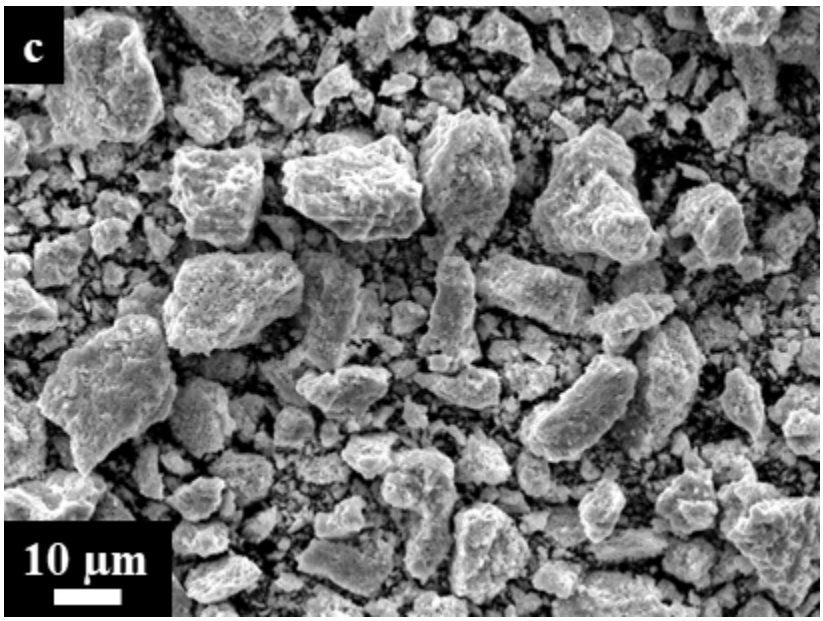

Figure 2. SEM micrographs for $Y_{0.7}Tb_{0.3}MnO_3$ powders: YTMO SS magnification a) 1000, b) 10000 and YTMO SG magnification c) 1000, d) 10000.

107x80mm (96 x 96 DPI)

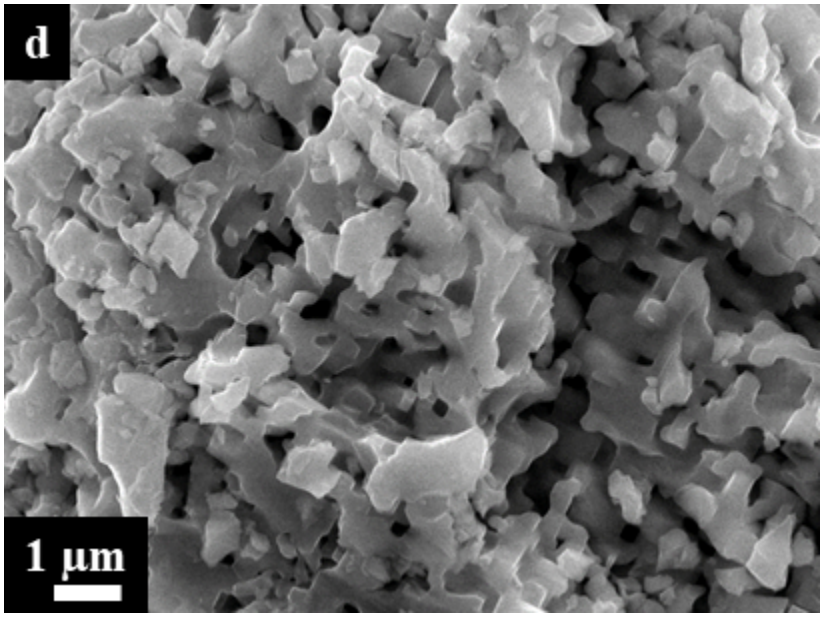

Figure 2. SEM micrographs for $Y_{0.7}Tb_{0.3}MnO_3$ powders: YTMO SS magnification a) 1000, b) 10000 and YTMO SG magnification c) 1000, d) 10000.

107x80mm (96 x 96 DPI)

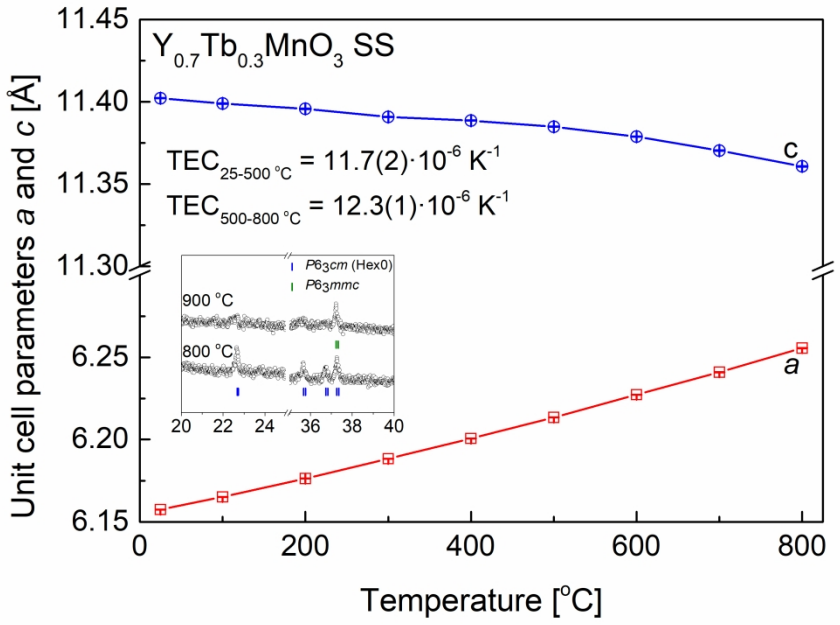

Figure 3. $Y_{0.7}Tb_{0.3}MnO_3$ SS: Temperature dependence of the unit cell parameters a and c of the Hex0 phase ($P6_3cm$) recorded on heating to 800 °C in air, together with the experimental values of TEC. Inset shows zoomed angular regions demonstrating change of the symmetry from $P6_3cm$ to $P6_3mmc$ at 900 °C.

288x201mm (300 x 300 DPI)

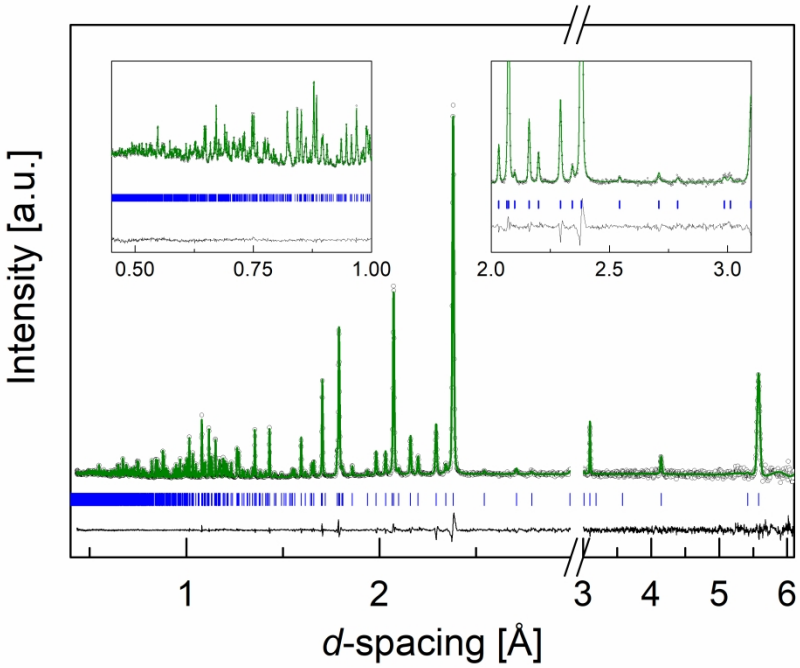

Figure 4. Best-fit Rietveld profile using the space group $P6_3mc$ (#186) of $Y_{0.7}Tb_{0.3}MnO_{3.45}$. Observed (plus sign) and calculated (red solid line) intensities are shown together with their difference at the bottom (blue solid line). Tick marks below the neutron diffraction pattern represent the Bragg peak positions for $P6_3mc$. Insets show zoomed in regions demonstrating the high quality of the fit. The small peaks in the right inset are extra reflections produced by the Hex3 $P6_3mc$ symmetry.

288x201mm (300 x 300 DPI)

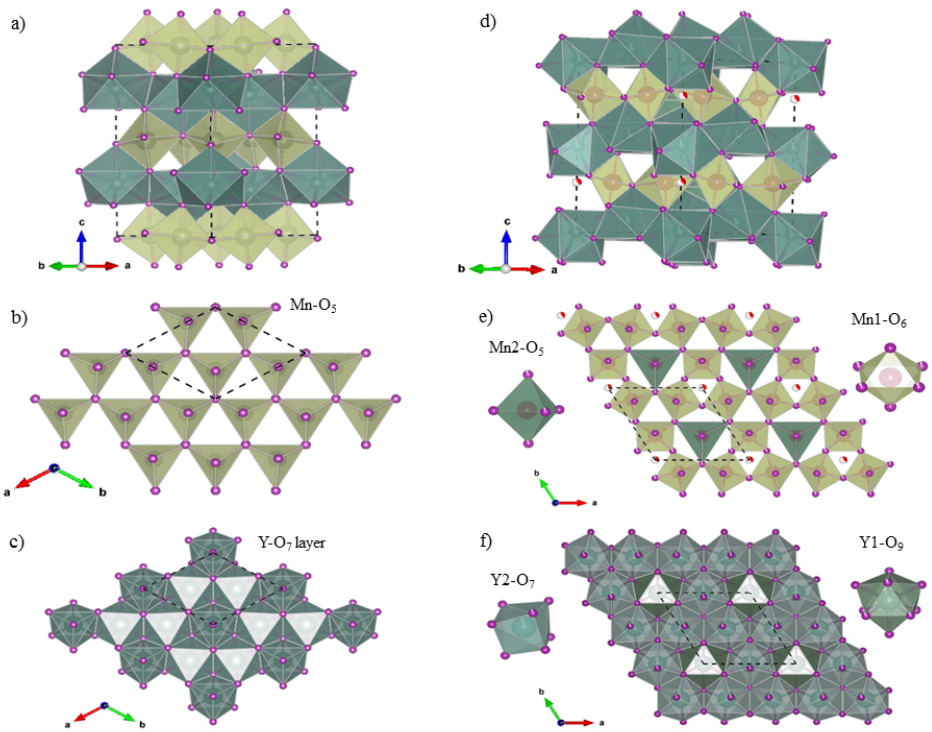

Figure 5. Left Panels: (a-c) Parent structure for oxygen stoichiometric Hex0 structures with space group $P6_3cm$ (#185). b) The structure consists of alternating layers of MnO_5 bipyramids and c) YO_7 polyhedra. Right Panels: (d-f) Structure of oxygen loaded $Y_{0.7}Tb_{0.3}MnO_{3.45}$ with space group $P6_3mc$ (#186). See text for more details.

254x190mm (96 x 96 DPI)

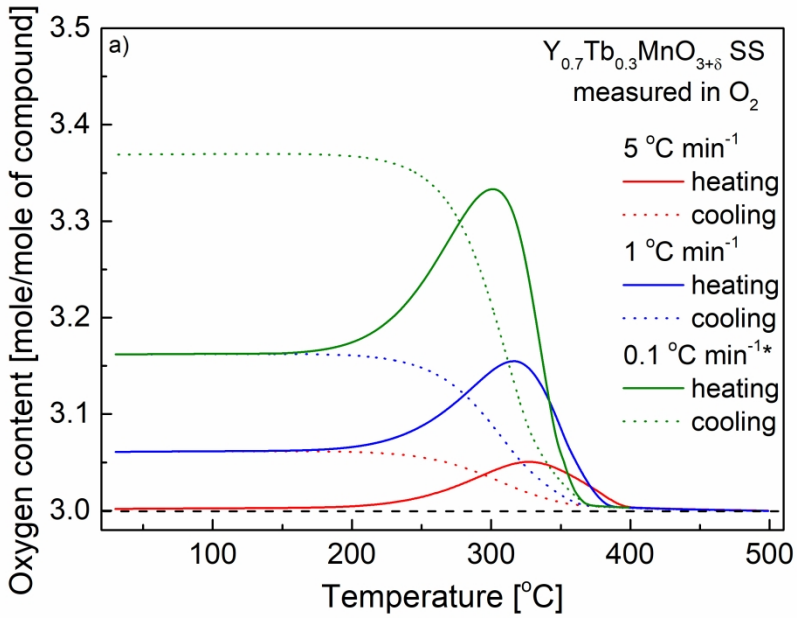

Figure 6. Temperature dependence of the oxygen content for a) $Y_{0.7}Tb_{0.3}MnO_{3+\delta}$ SS and b) $Y_{0.7}Tb_{0.3}MnO_{3+\delta}$ SG registered during heating and cooling in pure oxygen with heating rates of 5 °C min^{-1}, 1 °C min^{-1} and 0.1 °C min^{-1}.

288x201mm (300 x 300 DPI)

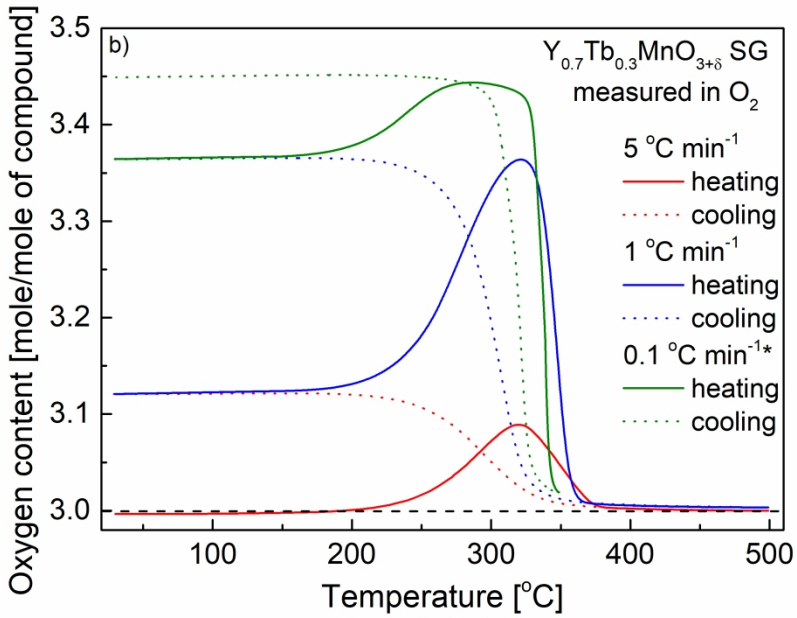

Figure 6. Temperature dependence of the oxygen content for a) $Y_{0.7}Tb_{0.3}MnO_{3+\delta}$ SS and b) $Y_{0.7}Tb_{0.3}MnO_{3+\delta}$ SG registered during heating and cooling in pure oxygen with heating rates of 5 °C min^{-1}, 1 °C min^{-1} and 0.1 °C min^{-1}.

288x201mm (300 x 300 DPI)

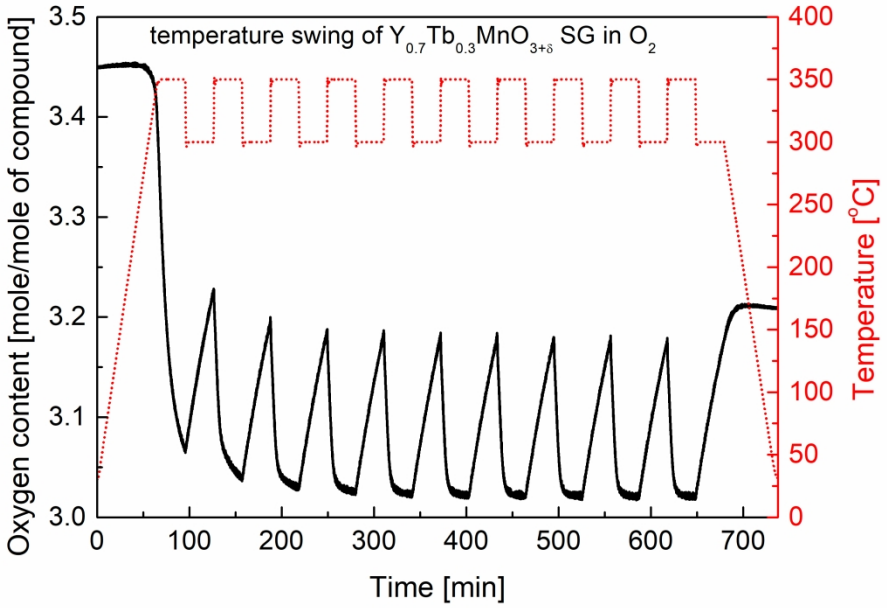

Figure 7. TSA process recorded for $Y_{0.7}Tb_{0.3}MnO_{3+\delta}$ SG in O_2 between 300 °C and 350 °C. Rapid heating and cooling of 100 °C min^{-1} was applied during the temperature change.

289x201mm (300 x 300 DPI)

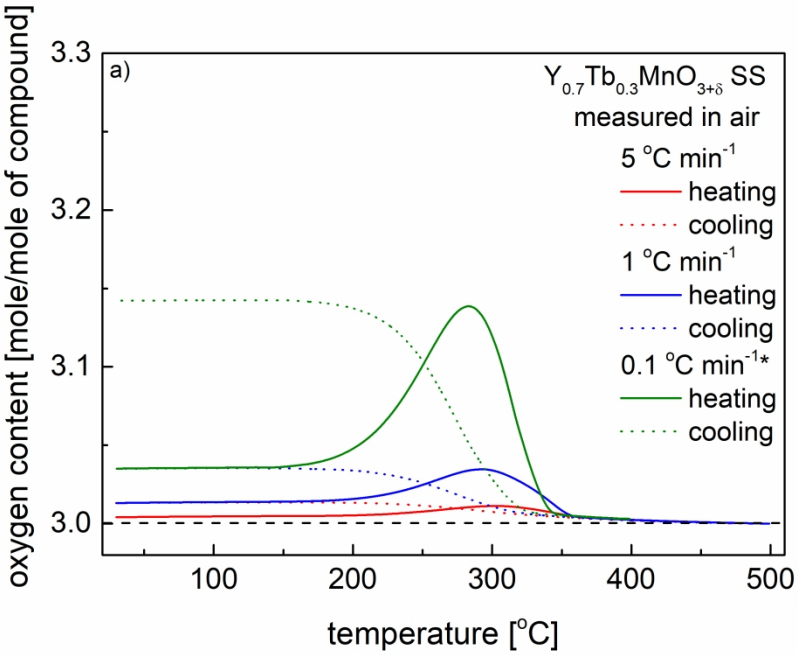

Figure 8. Temperature dependence of the average oxygen content for a) $Y_{0.7}Tb_{0.3}MnO_{3+\delta}$ SS and b) $Y_{0.7}Tb_{0.3}MnO_{3+\delta}$ SG registered during heating and cooling in synthetic air with heating rates of 5 °C min^{-1}, 1 °C min^{-1} and 0.1 °C min^{-1}.

288x201mm (300 x 300 DPI)

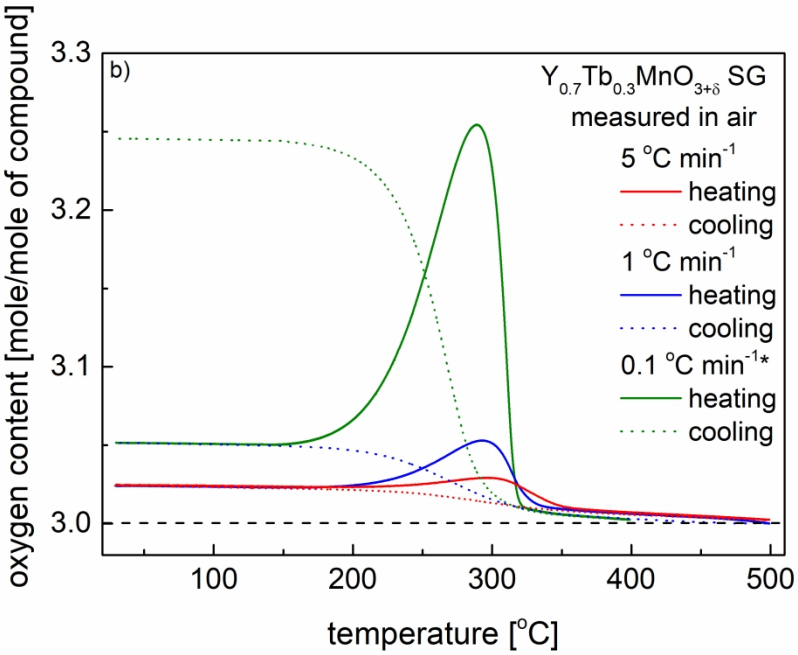

Figure 8. Temperature dependence of the average oxygen content for a) $Y_{0.7}Tb_{0.3}MnO_{3+\delta}$ SS and b) $Y_{0.7}Tb_{0.3}MnO_{3+\delta}$ SG registered during heating and cooling in synthetic air with heating rates of 5 °C min^{-1}, 1 °C min^{-1} and 0.1 °C min^{-1}.

288x201mm (300 x 300 DPI)

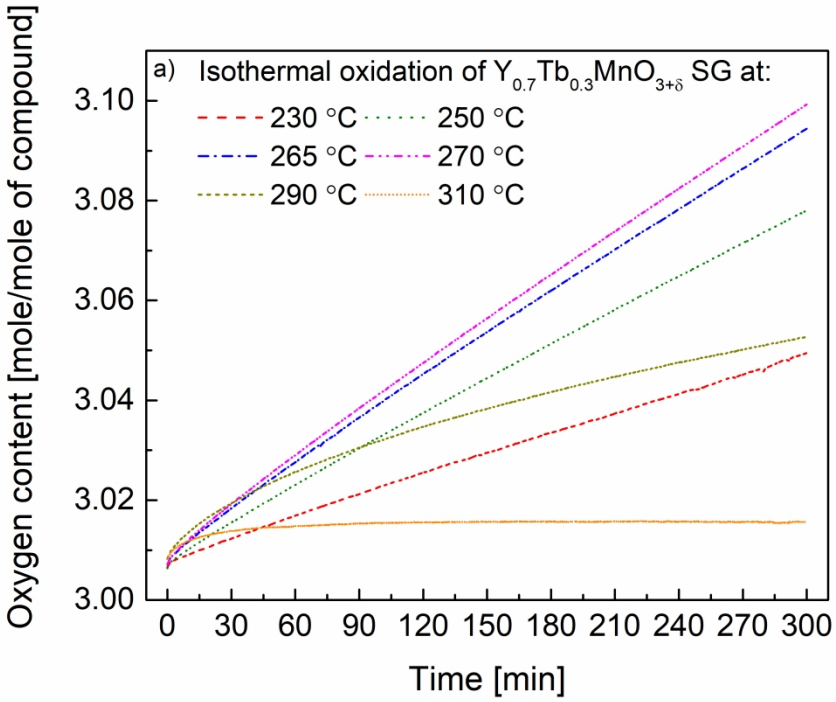

Figure 9. a) Isothermal oxidation of $Y_{0.7}Tb_{0.3}MnO_{3+\delta}$ SG in air at various temperatures and b) isothermal reduction in air registered at 330 °C after oxidation at temperatures 230 – 310 °C.

272x208mm (300 x 300 DPI)

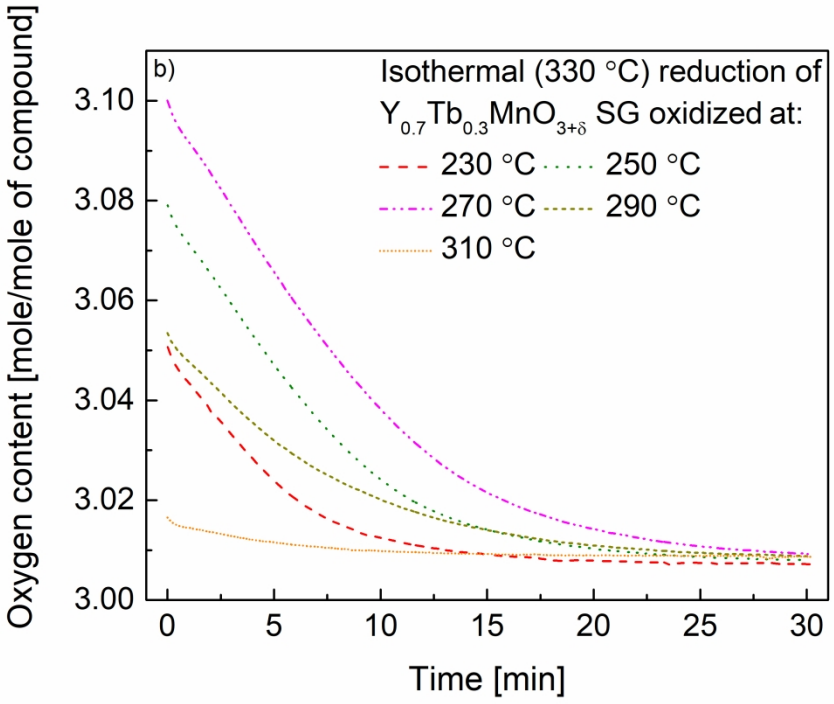

Figure 9. a) Isothermal oxidation of $Y_{0.7}Tb_{0.3}MnO_{3+\delta}$ SG in air at various temperatures and b) isothermal reduction in air registered at 330 °C after oxidation at temperatures 230 – 310 °C.

272x208mm (300 x 300 DPI)

Table 1. Select structural parameters for oxygen loaded $Y_{0.7}Tb_{0.3}MnO_{3.45}$.

Space group: *P*6$_3$*mc* (#186) Room temperature lattice Parameters: $a = b = 7.1575(2)$ (Å); $c = 11.1552(4)$ (Å); $\gamma = 120^o$ Unit cell volume= 494.92(3) (Å^3) Total Refined Oxygen Content = 3.45 R_{wp} =2.9%; R_I = 8.61%; χ^2 = 4.034								
Atom Type /Wyckoff Position	Fractional Occupancy	Fractional Coordinates			Anisotropic Thermal Factors (Å^2) 100 x			
		x	y	z	$U_{11} = U_{22}$	U_{33}	U_{12}	$U_{13} = -U_{23}$
$(Y/Tb)_1$ (2a)	0.93(2)	0	0	0*	0.29(6)	0.6(1)	0.15(3)	0
$(Y/Tb)_2$ (6c)	0.93(1)	0.4997(1)	0.5003(1)	0.5609(2)	0.29(4)	2.23(7)	0.19(4)	-0.16(2)
Mn_1 (6c)	1	0.8343(3)	0.1657(3)	0.7912(3)	0.92(8)	0.09(8)	0.67(9)	0.05(2)
Mn_2 (2b)	1	0.333333	0.666667	0.8053(8)	14.8(8)	-0.4(3)	7.4(4)	0
O1 (6c)	0.90(1)	0.1246(2)	0.8754(2)	0.8257(2)	0.67(6)	1.2(1)	-0.2(5)	-0.33(3)
O2 (6c)	0.92(1)	0.5293(2)	0.4707(2)	0.7702(2)	1.11(8)	1.1(1)	-0.35(6)	-0.24(3)
O31 (6c)	0.99(2)	0.8528(2)	0.1472(2)	0.6238(2)	0.90(6)	0.38(7)	0.56(6)	0.07(2)
O32 (6c)	1.00(2)	0.1858(2)	0.8142(2)	0.4603(3)	1.24(7)	0.44(7)	0.76(6)	-0.04(3)
O41 (2b)	1.05(2)	0.33333	0.66667	0.6455(3)	1.5(1)	0.5(1)	0.76(6)	0
O42 (2b)	1.01(2)	0.33333	0.66667	0.9704(4)	2.3(1)	0.6(2)	1.13(7)	0
O5 (2a)	0.35(5)	0	0	0.788(4)	9(1)	18(5)	4.3(9)	0

*The z position of (Y/Tb)1 was kept fixed to allow refinements with a known origin.

Table 2. Select bond-lengths for oxygen loaded $Y_{0.7}Tb_{0.3}MnO_{3.45}$.

(Y/Tb)1-O1 x 3	2.48323(6)	Mn1-O1 x 2	1.89295(6)
(Y/Tb)1-O31 x 3	2.28805(5)	Mn1-O2 x 2	1.93232(6)
(Y/Tb)1-O32 x 3	2.34496(7)	Mn1-O31 x 1	1.88137(6)
(Y/Tb)1-O5 x 1	2.36399(8)	Mn1-O32 x 1	1.90280(6)
(Y/Tb)2-O2 x 1	2.36356(8)	Mn1-O5 x 1	2.05498(7)
(Y/Tb)2-O31 x 2	2.30794(7)		
(Y/Tb)2-O32 x 2	2.25541(6)	Mn2-O2 x 3	2.46027(8)
(Y/Tb)2-O41 x 1	2.26760(6)	Mn2-O41 x 1	1.78273(6)
(Y/Tb)2-O42 x 1	2.30329(6)	Mn2-O42 x 1	1.84219(6)

Table 3. Oxygen storage-related properties of the studied oxides, measured in O_2 atmosphere.

Chemical composition	OSC between RT and 500 °C [wt.%]	Max. oxygen content during 0.1 °C min^{-1} heating in oxygen	Temperature of the max. oxygen content on 0.1 °C min^{-1} heating [°C]	ΔT [°C]
$YMnO_{3+\delta}$ SS*	1.33	3.14	230	33
$YMnO_{3+\delta}$ SS 15 MM*	1.84	3.20	230	37
$YMnO_{3+\delta}$ SG*	2.48	3.27	225	45
$HoMnO_{3+\delta}$ SS#	1.64	3.26	260	42
$HoMnO_{3+\delta}$ 15MM SS#	1.73	3.27	250	32
$DyMnO_{3+\delta}$ SS&	1.48			40
$Y_{0.7}Dy_{0.3}MnO_{3+\delta}$ SS&	2.26	0.27$	320$	110

$Y_{0.7}Tb_{0.3}MnO_{3+\delta}$ SS	2.70	3.33	331	25
$Y_{0.7}Tb_{0.3}MnO_{3+\delta}$ SG	3.27	3.44	286	19

* Data from [33]. # Data from [34]. & Data from [12], $ read from Fig. 1 [12]. Samples denoted as 15MM were additionally mechanically milled (MM) after the sintering process.

Table 4. Oxygen storage-related properties of the studied oxides, measured in synthetic air.

Chemical composition	OSC between RT and 500°C [wt.%]	maximum oxygen content during 0.1° min^{-1} heating	temperature of the max oxygen content on 0.1° min^{-1} heating [°C]	ΔT [°C]
$HoMnO_{3+\delta}$ SS 15MM [#]	0.50	3.08	235	35
$Y_{0.7}Tb_{0.3}MnO_{3+\delta}$ SS	1.06	3.14	283	37
$Y_{0.7}Tb_{0.3}MnO_{3+\delta}$ SG	1.81	3.25	289	23

[#] Data from [34]. Samples denoted as 15MM were mechanically ball-milled (MM) after the sintering process.